How Well Does an Earth System Model Represent the Occlusion of Extratropical Cyclones?

CATHERINE M. NAUD,[a] GREGORY S. ELSAESSER,[a] POUSHALI GHOSH,[b] JONATHAN E. MARTIN,[b] DEREK J. POSSELT,[c] AND JAMES F. BOOTH[d]

[a] *Applied Physics and Applied Mathematics, Columbia University, NASA GISS, New York, New York*
[b] *Atmospheric and Oceanic Sciences, University of Wisconsin–Madison, Madison, Wisconsin*
[c] *Jet Propulsion Laboratory, California Institute of Technology, Pasadena, California*
[d] *Department of Earth and Atmospheric Sciences, The City College of New York, New York, New York*

(Manuscript received 10 May 2024, in final form 23 December 2024, accepted 14 January 2025)

ABSTRACT: Extratropical cyclones are the main providers of midlatitude precipitation, but how they will change in a warming climate is unclear. The latest NASA Goddard Institute for Space Studies (GISS) Earth system models (ESMs) accurately simulate the location and structure of cyclones, though deficiencies in the depiction of cloud and precipitation are found. To provide a new process-level context for the evaluation of simulated cloud and precipitation in the midlatitudes, occluded cyclones are examined. Such cyclones are characterized by the formation of a thermal ridge, maintained via latent heat release in the wider three-dimensional trough of warm air aloft (TROWAL) in the occluded sector. Using a novel method for the objective identification of occluded cyclones, the simulation of occlusions in the latest GISS-E3 model is examined. The model produces occluded cyclones, adequately depicting the thermal and kinematic structures of the thermal ridge, with realistic depth and poleward tilt. Nevertheless, E3 occlusions are less frequent than observed and systematically shifted poleward and toward the exit region of the climatological storm tracks. Compared to *CloudSat–CALIPSO* cloud retrievals across the thermal ridge, the dependence of cloud properties on thermal ridge strength is well represented, though at the expense of producing low ice mass clouds too often at high altitudes (i.e., "too many, too tenuous"). Overall, E3 produces significantly more precipitation in occluded versus nonoccluded cyclones, demonstrating the importance of accurately representing occlusions and associated hydrological processes in ESMs.

KEYWORDS: Extratropical cyclones; Latent heating/cooling; Mesoscale processes; Potential vorticity; General circulation models; Model evaluation/performance

1. Introduction

The majority of the precipitation in the midlatitudes (30°–60°N/S) is delivered by extratropical cyclones and their attendant fronts, up to 80% in the winter (Hawcroft et al. 2012; Catto et al. 2012). These systems are also responsible for the most extreme precipitation events (Pfahl and Wernli 2012; Kunkel et al. 2012). As Earth's climate changes, concurrent changes in extratropical cyclones, their attendant precipitation distributions, and associated extremes are the subject of active research (e.g., Bengtsson et al. 2009; Pfahl and Wernli 2012; Kunkel et al. 2013; Marciano et al. 2015). Future climate predictions suggest an increase in the precipitation associated with extratropical cyclones (Zhang and Colle 2017), forced by changes in temperature and moisture availability (Yettella and Kay 2017), not so much by changes in cyclone strength (Sinclair and Catto 2023). In addition, many studies have shown the importance of latent heat release in areas of cloud and precipitation formation for cyclone development (Binder et al. 2016), but cloud and precipitation representation and their associated latent heating in Earth system models (ESMs) are still deficient (e.g., Catto et al. 2015; Naud et al. 2020). Therefore, the ESM representation of moist processes associated with extratropical cyclones needs to be further evaluated to increase confidence in future climate predictions.

One aspect of the cyclone life cycle that is strongly influenced by latent heat release is the occlusion process, whereby cyclones adopt a characteristic thermal structure as they reach their postmature phase. First introduced by Bergeron (Jewell 1981), the warm occlusion process involves the cold front encroaching upon, and eventually ascending, the warm frontal surface (due to static stability contrasts; Stoelinga et al. 2002). This promotes the production of a wedge of warm air aloft displaced poleward of the warm front. This warm wedge manifests as a thermal ridge between the cyclone center and the peak of the warm sector (Martin 1998a,b, 1999a,b; Schultz and Vaughan 2011; and references therein). Warm moist air is forced to ascend cyclonically from the warm sector boundary layer through the thermal ridge, predominantly via positive vorticity advection by the thermal wind (Sutcliffe 1947; Martin 1999a,b), filling a sloping three-dimensional region called the trough of warm air aloft (TROWAL) (Crocker et al. 1947; Penner 1955) with clouds and precipitation. It is in association with this feature, not the surface occluded front, that some of

Denotes content that is immediately available upon publication as open access.

Supplemental information related to this paper is available at the Journals Online website: https://doi.org/10.1175/JCLI-D-24-0252.s1.

Corresponding author: Catherine Naud, cn2140@columbia.edu

DOI: 10.1175/JCLI-D-24-0252.1

the heaviest precipitation observed in the occluded cyclone often occurs (Martin 1998b; Grim et al. 2007; Han et al. 2007; Naud et al. 2024). Therefore, the occluded thermal ridge (OTR) is the location of substantial latent heat release which, in turn, substantially shapes the tropopause-level potential vorticity (PV) and tropospheric thermal structure of the canonical warm occlusion (Posselt and Martin 2004). Thus, examination of the structure and evolution of occluded cyclones in an ESM indirectly contributes to the evaluation of the model's fidelity in representing latent heat release and its impacts. Focusing on occlusions, synoptic entities with an identifiable structure, and a well-understood synergistic relationship with cloud and precipitation production affords a real test of the fidelity of the model's representations of the component physical processes it hopes to replicate as well as their interactions.

To the authors' knowledge, there have been no prior studies that document the occurrence, the structure, or the evolution of occluded cyclones in ESMs. This is partly because, until recently, there was no automated method to identify occlusions in models. In Naud et al. (2023), such a method was designed and applied to the Modern-Era Retrospective Analysis for Research and Applications, version 2 (MERRA-2; Gelaro et al. 2017). The same method can be applied to any gridded dataset, observational or otherwise, thus making it suitable for application to ESMs, enabling novel process-level model evaluation. In this study, we apply the identification methodology to the Goddard Institute for Space Studies (GISS) latest Earth system model (GISS-E3). Using MERRA-2 and combined observations from *CloudSat* (Stephens et al. 2002) and *CALIPSO* (Winker et al. 2009) for reference, we evaluate E3's ability to represent occlusions, their structure, and their cloud properties in the OTR. This analysis is aimed at addressing the following questions: 1) Does an ESM represent the occlusion process? And 2) how well does it represent the thermal, kinematic, and cloud structures of the occluded cyclone? Additionally, we seek to demonstrate that examination of an evolving synoptic entity, like an occluded cyclone, which inherently depends on the interaction of scales ranging from the continental to the microphysical, can assist in identifying potential model deficiencies.

The examination of these issues is organized as follows. Section 2 presents details concerning the model and its integration, the datasets used for comparison, and the various tools needed for the intended analysis. The evaluation of the model's depiction of occlusions is detailed in section 3 and progresses from an examination of the large-scale environment within which the storms form to the cyclone scale and then finally to the thermal ridge scale. Section 4 includes a discussion on why and how an accurate representation of occlusions in E3 informs understanding of the model's depiction of precipitation distribution as well as extremes. A summary and conclusions are available in section 5.

2. Model, datasets, and methodology

This section describes the model to be tested, the various algorithms and tools employed throughout the analysis, and the datasets used for comparison.

a. The CMIP6 NASA Goddard Institute for Space Studies Earth system model E3

GISS-E3, the latest and most advanced of three GISS contributions to CMIP6 (E2.1, E2.2, and E3), is the focus of this study. Compared to the other two GISS models, E3 comprises substantial upgrades to multiple physical parameterizations, an increase in vertical resolution (from 40 to 110 layers), and the use of a machine learning algorithm to more objectively calibrate or "tune" the ESM (Elsaesser et al. 2024). An early summary of the physics upgrades relative to E2.1 is available in Cesana et al. (2019), and the particular tuned candidate known as "Tun2" is analyzed here in Cesana et al. (2021) and Li et al. (2023). A selection of the pertinent physical schemes that directly affect cloud and precipitation is summarized below:

- Planetary boundary layer physics: It includes novel heat flux equations without the use of a critical Richardson number (Cheng et al. 2020), along with the moist turbulence scheme based on Bretherton and Park (2009).
- Convection: The upgraded double plume model described in Kelley et al. (2020) for E2.1 was further modified to include cold pool representation (Del Genio et al. 2015) and improved ice microphysics (Elsaesser et al. 2017a).
- Large-scale cloud parameterization: A prognostic stratiform precipitation [Morrison-Gettelman (MG2) microphysics; Gettelman and Morrison 2015] and a new stratiform cloud fraction scheme (Smith 1990) were implemented.

In GISS-E3, ice water path (IWP) and liquid water path (LWP) are substantially decreased from previous versions of the model and in closer agreement with observational estimates (Elsaesser et al. 2017a,b). Substantial improvements in simulating convective phenomena are also noted (e.g., tropical cyclones; Russotto et al. 2022).

The current analysis utilizes an atmosphere-only free-running integration of E3, forced with prescribed transient, monthly varying sea surface temperatures. Our focus is on the 2006–11 period. We use the $2.5^\circ \times 2^\circ$ horizontal resolution configuration as in Cesana et al. (2019, 2021) and Li et al. (2023), although c90 ($\sim 1^\circ$) resolution will be the final resolution submitted to CMIP6. The 3-hourly model output includes two-dimensional sea level pressure and surface precipitation and profiles (on 110 vertical levels from 979 to 0.0035 hPa) of temperature, specific humidity, geopotential height, wind, vertical velocity, cloud fraction, and ice and liquid water content for both suspended and falling condensates. Because GISS-E2.1 is also part of the CMIP6 model ensemble, we performed a cursory evaluation of the occlusion depiction in this model (same horizontal resolution, but lower vertical resolution and substantially different cloud parameterizations; full details in Kelley et al. 2020) and summarized the results in the supplemental material document.

b. Tracking extratropical cyclones

To identify the location of extratropical cyclones and track their evolution in time, we use the algorithm of Bauer and Del Genio (2006). This algorithm, fully described and evaluated in Bauer et al. (2016), utilizes gridded sea level pressure

fields and searches for local minima. To briefly summarize, the algorithm first imposes thresholds for the central pressure and the difference in pressure relative to the surrounding area to decide whether the identified minima are indeed depressions. Upon identification, the candidate centers are tracked in time, with a number of thresholds imposed for the rate of change in central pressure and its maximum horizontal displacement (no more than 720 km in 6 h). At the end, a list of cyclone tracks lasting at least 36 h is generated, with information on the latitude and longitude of each center every 6 h from cyclone initiation to dissipation. This algorithm was applied and tested by Bauer et al. (2016) on the ERA-Interim reanalysis (Dee et al. 2011). The same tracking algorithm is applied to E3 sea level pressure fields, with cyclone information stored every 6 h for consistency.

c. *Identification of occlusions*

Using the cyclone track history obtained with the Bauer and Del Genio method, an occlusion identification algorithm, as described in Naud et al. (2023), is then applied. The algorithm searches for 6-hourly cyclone instances along each track with an occluded thermal ridge: a two-dimensional projection of the full three-dimensional TROWAL region. Using the 1000–500-hPa thickness ϕ' field, the thermal ridge is identified around each cyclone center (within ±20° latitude, from 10°W to 20°E) by assessing the divergence of the unit vector of the ϕ' gradient $\hat{n} = \nabla\phi'/|\nabla\phi'|$. Grid cells around the cyclone are flagged if 1) they indicate convergence [using $F = (\nabla \cdot \hat{n})|\nabla\phi'| < -1\,10^{-6}\mathrm{m}^{-1}$] and 2) they are not in regions of heterogeneous topography (standard deviation of surface altitude among nearest neighbors less than 300 m). Using the cyclone tracks, this cluster of flagged grid cells is tracked in time using a cyclone-centered grid if at a minimum it encompasses four grid cells at the 2.5° × 2° resolution of the model. If these converging regions spatially overlap in time in this reference grid for at least two consecutive 6-h time steps, and the period over which the overlap occurs contains or follows the time of maximum cyclone intensity (i.e., minimum in sea level pressure at the center over the entire lifetime), the cyclone track and the individual 6-hourly instances are identified as being occluded. This algorithm when applied to model E3 takes into account its 2.5° × 2° spatial resolution (cf. Naud et al. 2023).

d. *Reanalyses and CloudSat–CALIPSO for reference datasets*

The analysis presented below conducts a step-by-step evaluation of E3 and utilizes different reference datasets along the way. To evaluate E3 cyclone locations, we use the ERA-Interim database first created by Bauer et al. (2016), called the Modeling, Analysis, and Prediction (MAP) Climatology of Midlatitude Storminess (MCMS). A new version of the cyclone track database is being developed using the same algorithm applied to the more recent ERA5 reanalysis (Hersbach et al. 2020), but this database was not ready at the time of this work. Because cyclones tend to occur on the polar side of the upper-level jets, for consistency, ERA-Interim 250-hPa zonal winds are also used. These are the only tests that make use of ERA-Interim, and any other test that requires information typically provided with a reanalysis makes use of MERRA-2 (Gelaro et al. 2017) instead. This choice was motivated by its relative novelty compared to ERA-Interim and its relatively higher spatial resolution.

Using the MCMS cyclone tracks, we obtained MERRA-2 thickness fields for each 6-hourly cyclone instance and applied the algorithm described in the previous section to these. Therefore, we will refer to this subset of cyclones identified as occluded as the MERRA-2 database of occluded cyclones. This publicly available database of occluded cyclones was produced for the period 2006–17 and provides the list of cyclone instances that are occluded as well as the location of the thermal ridge. A full description of this database is provided in Naud et al. (2023), and the only difference here is that the MERRA-2 thickness fields were coarsened to a 2.5° × 2° resolution first, to match E3 spatial resolution. This modified MERRA-2 occluded cyclone collection serves as our observational compositing reference. Additionally, all the analyses that explore the environmental characteristics of E3 occluded cyclones use for comparison MERRA-2 6-hourly profiles of geopotential height, temperature, wind, specific humidity, and vertical velocity, available at 0.625° × 0.5° horizontal resolution on 42 levels from 1000 to 0.1 hPa.

To characterize cloud properties, we appeal to remotely sensed observations: specifically employing the *CloudSat–CALIPSO* geometric profile (GEOPROF)-lidar (Mace et al. 2009; Mace and Zhang 2014) and level-2C ice cloud property product (2C-ICE) (Deng et al. 2010) products as the sources for observed cloud hydrometeor states in cyclones. The GEOPROF-lidar product combines hydrometeor identifications from both the radar and the lidar and provides the location of up to five cloud layer bases and top heights in the *CloudSat* footprint (~1.3 km × 1.7 km). However, because *CloudSat* cannot distinguish falling from suspended particles, these cloud layers are more appropriately termed "hydrometeor layers." We use the altitude information on cloud layer bases and tops to create a vertical profile of hydrometeor presence, which indicates whether cloud and/or precipitation are present at 250-m resolution in the vertical.

The 2C-ICE product provides ice water content profiles obtained using both lidar 532-nm attenuated backscatter and radar reflectivity profiles ingested into an optimal estimation algorithm. These profiles are provided at the resolution of the *CloudSat* horizontal footprint (1.4 km across × 1.7 km along track). The uncertainty in retrieved IWC is estimated to be less than 30% (Deng et al. 2013), although that estimate might be substantially larger in precipitating clouds and with increasing convective core vertical depth (i.e., in the tropics). The reported IWC has a minimum threshold that is dictated by limits in both lidar and radar detectability. However, the model does not have such limitations and will provide very small values of IWC that are currently unobservable. To ensure a fairer comparison, we define a minimum IWC for use in E3 evaluation that best matches the retrieval capability. For this, we constructed a temperature-dependent threshold on IWC based on a 10-granule collection of 2C-ICE retrievals, informed by data analysis provided by M. Deng (2022, personal communication). The threshold $\mathrm{IWC}_{\mathrm{min}}$ is computed as follows:

$$\mathrm{IWC}_{\min} = 10^{-3.26474}, \text{where } T \le 210 \text{ K},$$

$$\mathrm{IWC}_{\min} = 10^{[(T-276.543)/20.3823]}, \text{where } T > 210 \text{ K},$$

where T is the temperature of each model grid cell level. The E3 IWC is set to zero in any grid cell level where $\mathrm{IWC}(T) < \mathrm{IWC}_{\min}$. Tests reveal a notable difference in mean IWC without incorporation of thresholding, with E3 estimates closer to observations upon application of the threshold.

e. *Compositing methodology*

To facilitate a comparison between E3 and MERRA-2 occluded cyclones, we developed a compositing methodology that enables the use of sparse datasets and provides useful insight on occlusion characteristics (Naud et al. 2023, 2024). Two types of geometric reference frames are used: One is a plan view that considers the cyclone as a whole and uses the cyclone center as an anchor for averaging various fields, while the other focuses on vertical transects across the thermal ridge.

For the cyclone-centered composites, the gridded fields are first projected onto a rectangular grid with meridional and zonal directions expressed in distance from the cyclone center, centered on the point of minimum in sea level pressure, with maximum dimensions ±4000 km west–east and ±3000 km south–north. The regridded fields from each cyclone are then superimposed before calculating the mean of all cyclones. Note that we do not apply any rotation on the cyclone fields to take account of the direction of propagation.

For the vertical transect composites, the thermal ridge serves as the anchor. The algorithm described in section 2c identifies the thermal ridge in each occluded cyclone as a set of contiguous points at which $F = (\nabla \cdot \hat{n})|\nabla \phi'|$ is smaller than a threshold value (-1×10^{-6} m^{-1}). A regression line (in latitude/longitude) is then calculated through this cluster. This line represents the orientation of the thermal ridge axis. At the median longitude of this thermal ridge axis, a transect line is drawn perpendicular to it. Finally, the thermal ridge axis line is slid along the transect line until it reaches the coincident 700-hPa θ_e maximum [hereafter referred to as max(θ_e)]. The location of this maximum is the anchor for the composites (see Naud et al. 2023 for additional details). As in Naud et al. (2023), we use max(θ_e) throughout as a metric to categorize the thermal ridges (from "cold" to "warm").

For MERRA-2 and the GISS models, geopotential heights, θ_e, and vertical velocity profiles—and, for E3 only, cloud fraction and IWC profiles—are aggregated along the perpendicular line using the nearest neighbor approach and arranged into distance bins of 200-km width from 1500 km on the equator-west side of the ridge to 1500 km on its polar-east side. Using the location of max(θ_e) at 700 hPa as the zero point, the perpendicular transects of all the thermal ridges are superimposed and their average was calculated.

For the composite transects that involve the use of the *CloudSat–CALIPSO* retrievals, the method has to be altered since the orbits provide data in random locations around the thermal ridges. A full description of the approach adopted is available in Naud et al. (2024; see their Fig. 2). In this case, all observational profiles (i.e., hydrometeor masks and ice water mass) in a broader region are used, as long as they are located between the two perpendiculars at the ridge extremities within ±1500 km of any point along the ridge. In this case, the closest point along the ridge to each observed profile is used as the anchor to obtain the distance information needed to populate transects. The effect of this random sampling of the entire ridge area as opposed to a simple perpendicular at the median longitude along the ridge was tested in Naud et al. (2024), and good agreement was found when this was applied to MERRA-2 θ_e profiles (cf. their Fig. 3).

3. Evaluation of occlusions in model E3

For the analysis of occlusions in E3, we first focus on the Northern Hemisphere (NH) winter season (December–February) for the 5-yr period of 2006–11. This hemisphere and season have been the foci of active research on occlusions, so there is ample literature providing additional references. Our prior experience suggests that 5 years is of sufficient duration to furnish a large, representative sample size without incurring an undue burden in terms of data storage.

a. *Are there occluded cyclones in E3?*

As discussed in section 2a, the model E3 integration is performed using prescribed sea surface temperatures (free running, with no nudging). Therefore, the cyclones that emerge in the model are not expected to match, in time and space, those that occurred in the real world. However, since the simulated climate presumably resembles the actual climate, extratropical cyclones are expected to collectively occur in places and at times that are comparable to reanalysis datasets. The first step, as a result, is to examine how closely the storm track and climate of E3 match those obtained with ERA-Interim for the same period of time. This first comparison includes all cyclones identified and tracked over both land and ocean.

Cyclones tend to congregate in regions referred to as the storm tracks (e.g., Hoskins and Hodges 2002, for the NH), which are typically found between Japan and Alaska in the North Pacific basin and between the U.S. Carolina coastline and Norway in the Atlantic Ocean. The ERA-Interim reanalysis indicates two hotspots for the 2006–11 winters (Fig. 1a): one off the east coast of southern Greenland and another along the Alaskan south coast. These were also reported in Hoskins and Hodges (2002) and Neu et al. (2013). The Mediterranean storm track is relatively weak, possibly because the tracker uses sea level pressures which, according to Hoskins and Hodges (2002), tend to miss small systems, such as those typically found in this region, that are more effectively identified using measures such as 850-hPa vorticity.

Model E3 represents the location of the NH winter storm tracks realistically (Fig. 1b) but with some notable differences. The total number of cyclones is close to that observed for the entire hemisphere, but E3 1) tends to have more cyclones occurring near the exit of the Atlantic storm track than the reanalysis, 2) does not produce sufficient cyclones

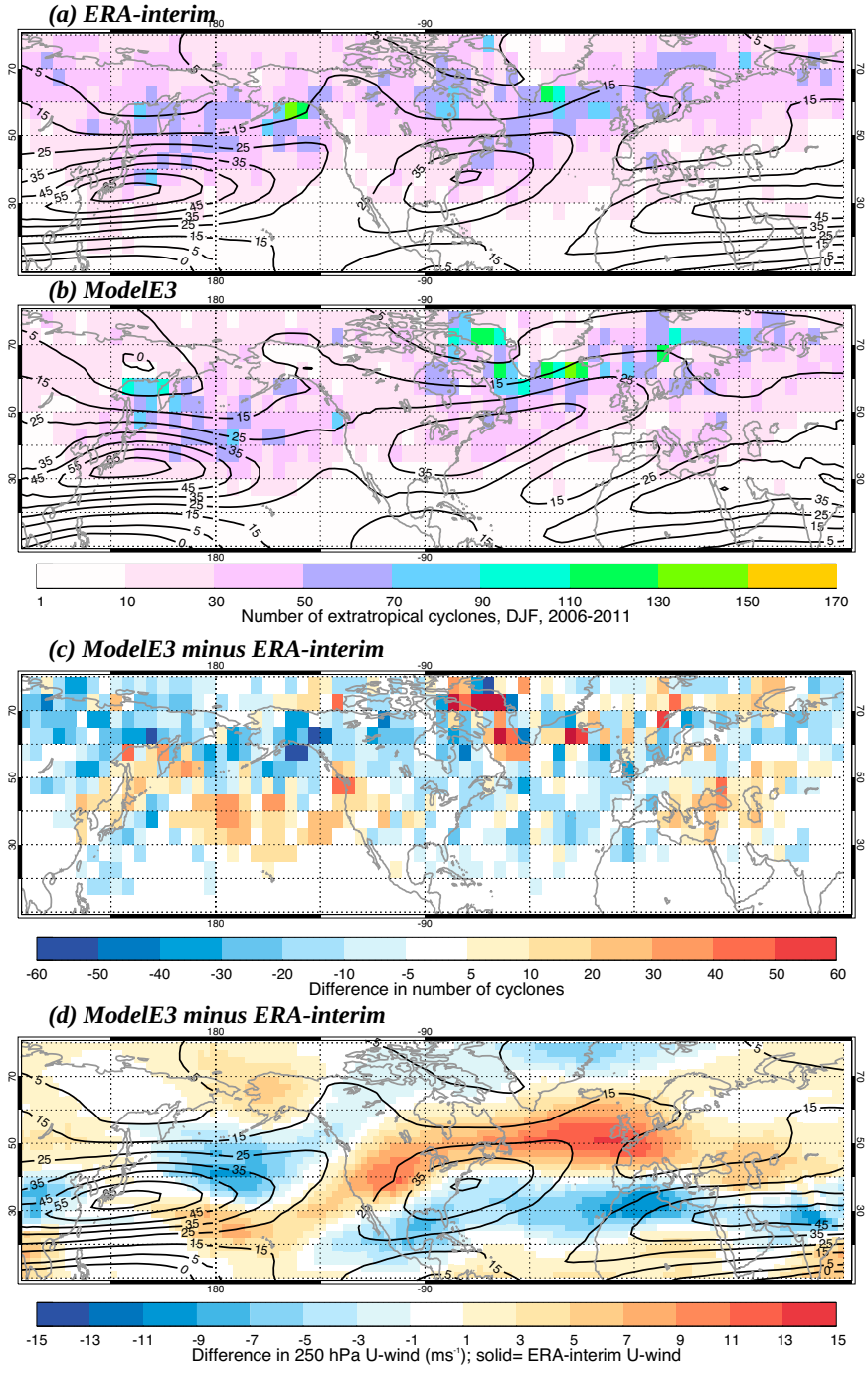

FIG. 1. Number of extratropical cyclone centers in 5° × 5° regions (color, from 1 to 160 in increments of 10) that occurred in December–February 2006–11 in (a) ERA-Interim and (b) model E3, with black contours showing the corresponding zonal wind speed at 250 hPa (from 5 to 65 m s^{-1}, every 10 m s^{-1}); (c) the difference in number of cyclones between model E3 and ERA-Interim (color, from −60 to 60, in increments of 10); and (d) the difference in 250-hPa zonal wind between model E3 and ERA-Interim for the same period (color, from −15 to 15 m s^{-1} every 2 m s^{-1}). The black solid contour in (d) shows the 250-hPa ERA-Interim zonal wind, in 10 m s^{-1} increments from 5 to 65 m s^{-1}.

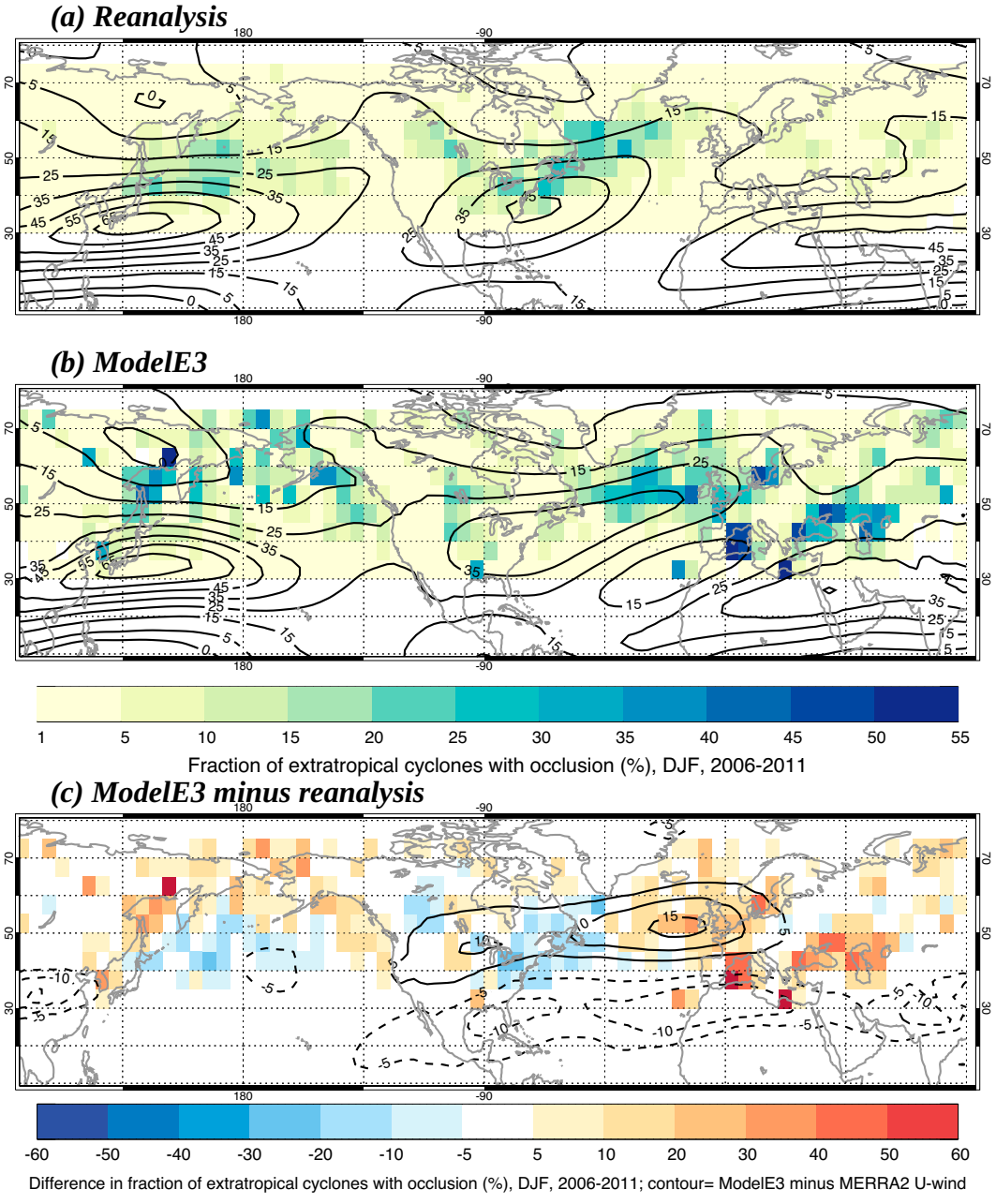

FIG. 2. Fraction of all cyclones per 5° × 5° cell that are identified as being occluded in (a) the reanalysis and (b) model E3 (%; in color, from 1% to 55% in 5% increments). The solid contours indicate the 250-hPa zonal wind averaged for times when an occluded cyclone occurs (m s^{-1}; from 5 to 65 m s^{-1} in 10 m s^{-1} increments). (c) The corresponding difference between model E3 and MERRA-2. Solid (dashed) contours show the difference in 250-hPa zonal wind between model E3 and MERRA-2 collected at the time of occlusion from 5 to 15 m s^{-1} (from −15 to −5 m s^{-1}) in 5 ms^{-1} increments.

along the coast of Alaska and the Pacific storm-track exit region generally, and 3) produces too many along the entire southern coast of Greenland. Overall, the preferred storm locations in the model's Atlantic basin tend to be found poleward of those in the reanalysis and equatorward in the Pacific basin (Fig. 1c). These shifts are consistent with the differences in the upper-level jet, expressed as the mean zonal wind at 250 hPa in Fig. 1d.

With these climatological differences in mind, we next examine the location of the occluded cyclones. Here, we consider all cyclone instances that are flagged as occluded, including those that belong to the same track. Then, we consider the fraction of

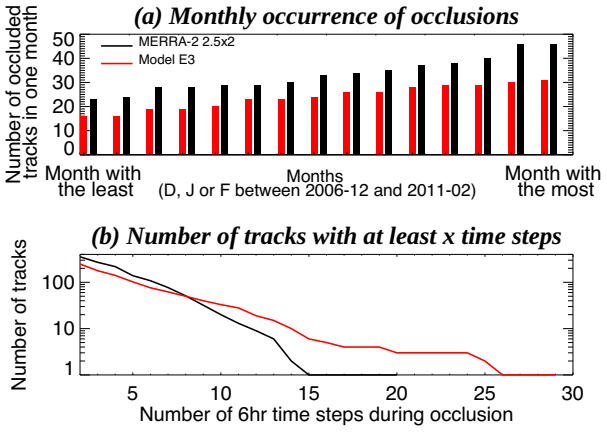

FIG. 3. (a) Number of tracks that are at some point occluded, per month, arranged from least to most populated (December, January, or February between December 2006 and February 2011) for MERRA-2 (black; 500 tracks in total) and model E3 (red; 359 tracks in total) and (b) the total number of tracks with a minimum number of 6-hourly time steps from 2 to 30 in MERRA-2 (black) and model E3 (red solid).

all cyclone instances in a 5° × 5° region that is identified as occluded over both land and ocean (cf. Fig. S1 in the online supplemental material for the actual numbers). For reference, in each box, we calculate the ratio of occluded cyclones, as identified with MERRA-2 thickness fields, to the total number of cyclones in the MCMS database. In this reference dataset, the fraction of occluded cyclones tends to be relatively larger in the entrance and middle regions of the storm track (middle and exit of the 250-hPa jets) in both ocean basins (Fig. 2a) consistent with the fact that occlusions develop preferentially in the left exit quadrant of the upper-level jets. As a result, there are relatively larger fractions to the west of the date line than to the east in the Pacific and west of Iceland rather than east of it in the Atlantic. However, the fraction of occluded cyclones in E3 exhibits some clear discrepancies with respect to reanalysis, in both ocean basins (Fig. 2b). In the Pacific, the occlusions are more evenly distributed and noticeably more frequent along the Alaskan coast in E3 than in the reanalysis. In the Atlantic Ocean, they tend to occur more frequently toward the exit region of the storm track than they do in the reanalysis. Cyclones also occlude in the Mediterranean Sea 45% more often in model E3 than in the reanalysis, though the physical basis for this notable discrepancy is unknown. Figures 2a and 2b also show the corresponding 250-hPa zonal winds averaged for all time steps when an occluded cyclone was identified. In Fig. 2a, we now use MERRA-2 winds for consistency with the occlusion identification (differences between MERRA-2 and ERA-Interim zonal winds are much smaller than between reanalysis and E3; see Fig. S2). While differences in jet location and in fraction of occluded cyclones appear to be collocated in the Atlantic basin (Fig. 2c), this is not the case in the Pacific basin or Mediterranean region. Therefore, differences in the large-scale circulation climatology alone do not explain differences in where occlusions are favored in E3.

Examining the occluded portion of the cyclone life cycles more specifically, we find there are fewer cyclones undergoing occlusion in E3 than in reanalysis (Fig. 3a). Figure 3a also reveals a larger variability in the number of occluded cyclones per month in MERRA-2 than in E3. However, for those cyclones that do occlude, they retain an occluded structure for a longer period of time in E3 (many for well over 3 days; Fig. 3b). It is clear that model E3 simulates occluded cyclones, but disparities with reanalysis in their preferred location, frequencies, and duration call for an exploration of the structure of the occluded cyclones in E3. Are the mechanisms involved in the occlusion process realistically represented?

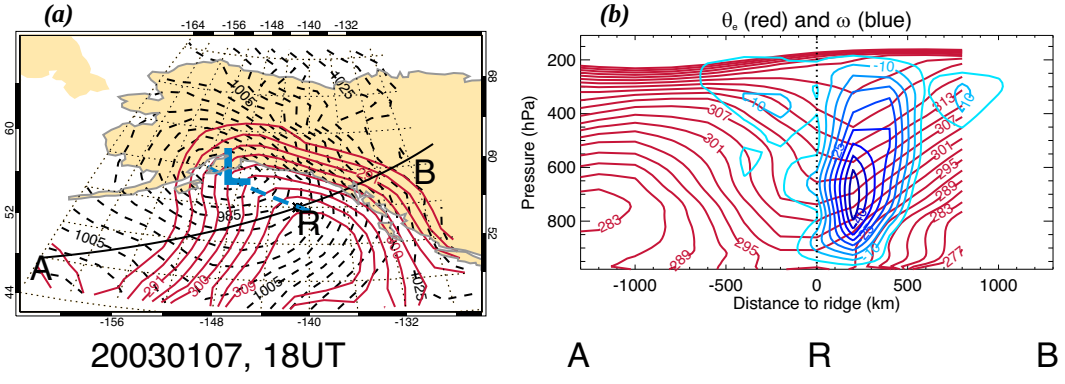

FIG. 4. An exemplar of an occluded cyclone simulated in E3 centered at 58.06°N and 149.91°W. (a) Plan view of the sea level pressure field (dashed contour, from 970 hPa in 4-hPa increments) and the 700-hPa equivalent potential temperature θ_e field (solid red, from 270 K, in 3-K increments), with the dashed blue line representing the OTR at 700 hPa and the solid black line representing a transect from A to B perpendicular to the thermal ridge with an intersect at *R*; (b) the vertical transects from A to B along the perpendicular to the ridge of θ_e (red contours, from 260 K, in 6-K increments) and vertical velocity where ascending (blue contours, from −45 hPa h^{-1}, in 5-hPa h^{-1} increments) as a function of the distance to the ridge intersect at 700 hPa (R) in 200-km increments. The vertical dotted line indicates the location of the ridge at 700 hPa.

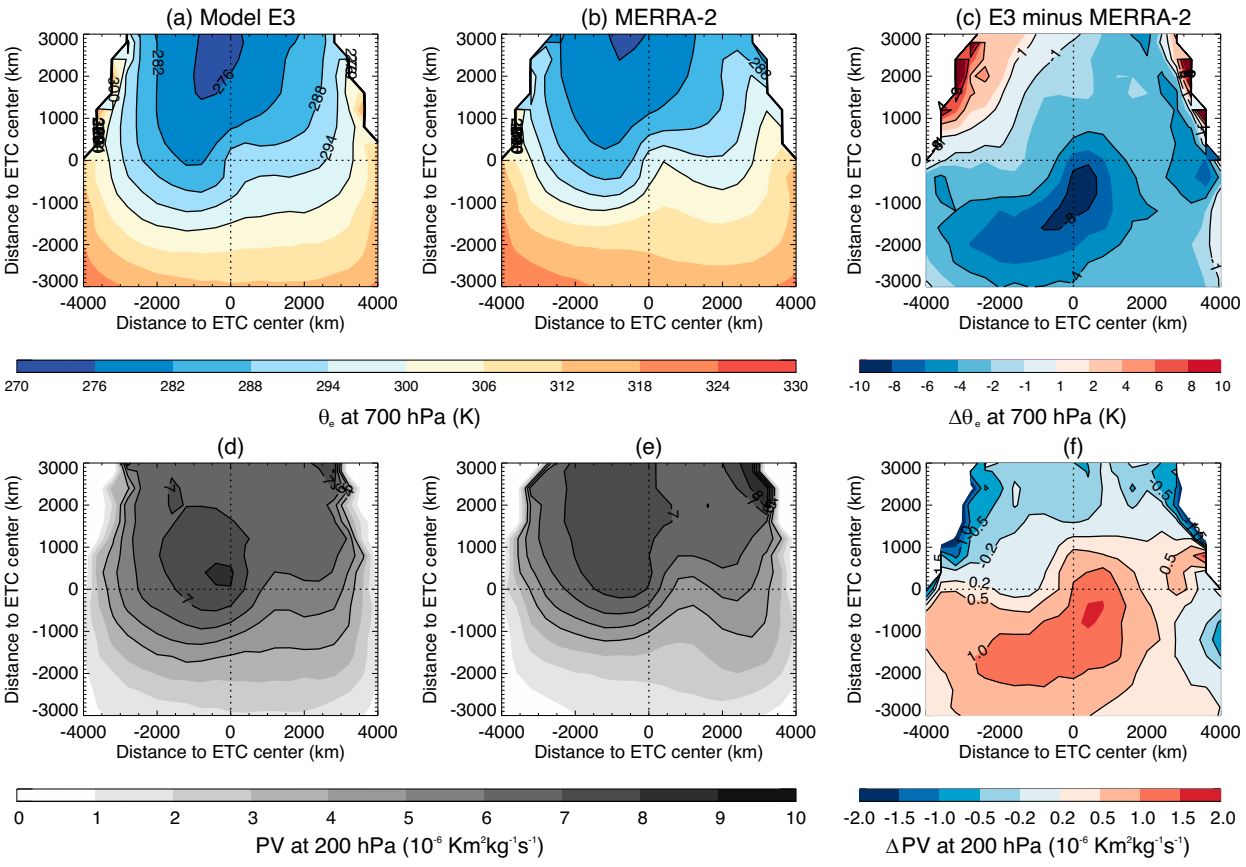

FIG. 5. Cyclone-centered composites of (a),(b) equivalent potential temperature at 700 hPa in model E3 and MERRA-2, respectively, with (c) the difference between the two; and cyclone-centered composites of (d),(e) 200-hPa PV for model E3 and MERRA-2 with (f) the difference between E3 and reanalysis. The dotted lines intersect at the cyclone center.

b. *Is the structure of the occluded cyclones in E3 realistic?*

An example of an occluded cyclone in E3 is first examined. Figure 4 provides the 700-hPa θ_e distribution around the cyclone center and across the OTR. As is typical of occluded cyclones, the θ_e field indicates an area to the east of the cyclone center with relatively large values, reflecting the location of the warm and moist airstream that wraps itself cyclonically around the cyclone center (Fig. 4a). Joining the inflection points of each θ_e contour establishes the general location of the OTR (dashed blue line). The vertical transect perpendicular to the ridge (A–B line in Fig. 4a) reveals the presence of a poleward sloping axis of maximum θ_e that coincides with a strong ascent, both typical of the thermal ridge (Fig. 4b; cf. Martin 1998a).

To assess whether this example is representative of most occlusions in E3, we build cyclone-centered, plan-view composites of 700-hPa θ_e for all DJF NH cyclones with a center over the ocean in E3 and MERRA-2, along with similarly constructed composites of the potential vorticity at 200 hPa (Fig. 5). These composites are constructed only for the time of maximum intensity during occlusion—that is, when any given occluded cyclone experiences its lowest sea level pressure. This is to avoid analysis issues that might arise from differing occlusion longevities (cf. Fig. 3b) and to ensure both sets of cyclones are as representative of a typical occlusion as possible. Because of topography, both cyclone tracking and occlusion identification algorithms may yield artifacts and result in larger uncertainties over land. Furthermore, the representation of topography in models is affected by the underlying spatial resolution. Therefore, from this point forward, E3's evaluation only considers the subset of cyclones whose centers reside over open ocean.

The 700-hPa θ_e composites show the typical contrast between the warm moist southerly flow and the cold dry northerly flow, with a sharp gradient at the cyclone center and a tongue of relatively higher θ_e expanding from southeast to northwest just east of the cyclone center, i.e., the thermal ridge. While model E3 realistically represents the overall thermal structure of the occluded cyclones at their peak intensity, the simulated cyclones have lower θ_e values at the center and less well-defined thermal ridges (Fig. 5a vs Fig. 5b; Fig. 5c).

The cyclone-centered composites of PV reveal a sharp gradient from west to east across the cyclone center, with a maximum in PV just to the northwest of the cyclone center and a tongue of relatively low PV to the east. Previous research has demonstrated that strong latent heat release in the thermal

ridge erodes the relatively high PV region in that vicinity, leading to the development of a low PV trough there (Martin 1998a; Posselt and Martin 2004). As described in Martin (1998a), in individual cyclones, the PV maximum close to the cyclone center is connected to a high PV reservoir at higher latitudes through a narrow filament making the PV distribution resemble a treble clef structure. Such a structure could be seen for randomly selected cyclones (not shown); however, in the MERRA-2 composite, the filaments do not align across all cyclones, smearing the treble clef pattern, resulting in a relatively wide area of high PV expanding poleward from just northwest of the cyclone center instead (Fig. 5e). While the E3 composite of PV (Fig. 5d) shares similarities with that from MERRA-2, the PV trough to the east of the cyclone center, like the simulated 700-hPa θ_e thermal ridge in Fig. 5a, is less well defined. Therefore, while the model provides a realistic thermal and kinematic structure at both lower and upper levels, respectively, the composite differences compel further examination of the thermal ridge, with a focus on clouds.

c. *How well are thermal, kinematic, and moisture variables represented in the E3 thermal ridge?*

To examine the thermal ridge structure, we construct and analyze vertical transect composites across the thermal ridge as described in section 2e. Discrepancies in the statistical location of the occluded cyclones in E3 relative to MERRA-2 cause differences in the mean cyclone-centered θ_e and PV distributions that tie more to mean state climatology misrepresentation and less to cyclone-specific feature differences. To better judge whether the vertical structure of the OTR is well represented in the model, we elect to conduct the ridge comparison between E3 and reanalysis for similar cyclones. To begin, we sort all occluded cyclones according to their max(θ_e) at 700 hPa along the thermal ridge. In this manner, we facilitate a fairer comparison of the E3 composite transects of θ_e and ω with MERRA-2 for similar thermal ridges. This is achieved by dividing the entire population of thermal ridges into three equal size subsets, using the same max(θ_e) thresholds for both the model and reanalysis. A sufficient sample size per max(θ_e) category is afforded by expanding the analysis of maritime cyclones to include both hemispheres and all seasons.

Next, we use *CloudSat–CALIPSO* overpasses of thermal ridges to obtain an independent view of hydrometeors across thermal ridges. The narrow swath of the instruments means that only a subset of all thermal ridges can be observed. To overcome this limitation, we use the full 2006–17 period with observations to ensure a large enough sample size in our reference dataset. Since the model provides complete information for all thermal ridges, for E3, we investigate the same 5-yr dataset used in earlier described analyses. We find that both E3 and the expanded observational dataset (MERRA-2 occlusions with *CloudSat–CALIPSO* overpasses) share a very similar distribution of max(θ_e) at 700 hPa across all OTRs (Fig. 6a), with slightly cooler cases in E3 for the NH (Fig. 6b) and warmer ones for the Southern Hemisphere (Fig. 6c) relative to MERRA-2.

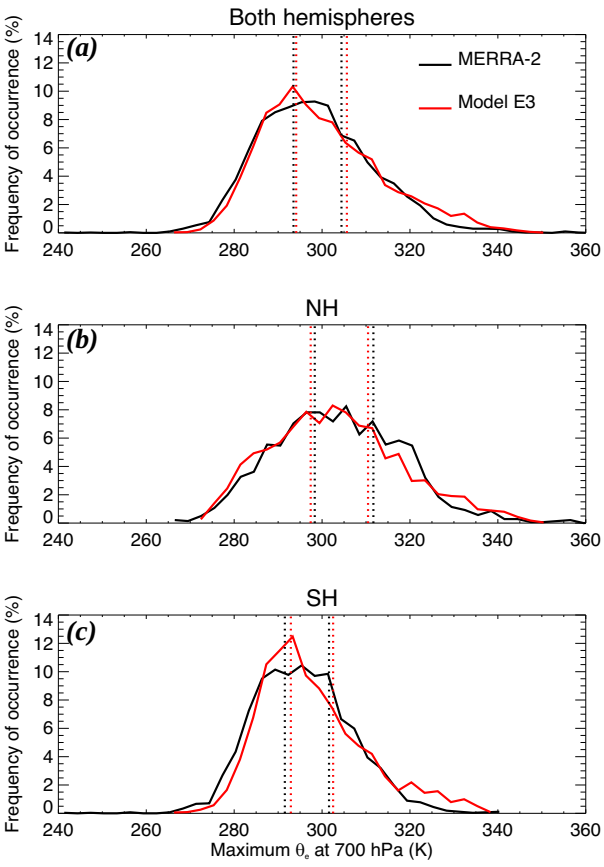

FIG. 6. Distribution of max(θ_e) at 700 hPa in all thermal ridges for all seasons (a) in both hemispheres, (b) in the NH only, and (c) in the Southern Hemisphere only, for MERRA-2 (black) and model E3 (red). The dotted lines indicate the θ_e values that divide the populations into three equal size subsets (red for model E3 and black for MERRA-2).

Using the entire population, the three max(θ_e) categories are defined as ridges with 1) $\theta_e < 294$ K, 2) $294 < \theta_e < 304$ K, and 3) $\theta_e > 304$ K. These are the categories we anchor against for all the thermal ridge transect comparisons.

Composite transects of θ_e and vertical velocity ω across the thermal ridge (Fig. 7) confirm that the single case of Fig. 4 is representative of the general E3 OTR structure. For each max(θ_e) category, E3 thermal structures across the thermal ridge are realistic, albeit not as well defined as their MERRA-2 counterparts, with E3 simulating comparable variation in θ_e transects from one max(θ_e) category to the next. The "warmest" category exhibits the closest match to the canonical structure of a warm occluded thermal ridge as discussed in Naud et al. (2023), and it is realistically represented by E3 (Fig. 7c vs Fig. 7f).

While E3 is also comparable to MERRA-2 with respect to ω, with a maximum slightly poleward of the thermal ridge, a clear vertical expansion, and increased tilt with increasing max(θ_e), the maximum in ascent strength is lower in the model, with differences in maximum ω at the ridge of at least 2 hPa h^{-1} [for the

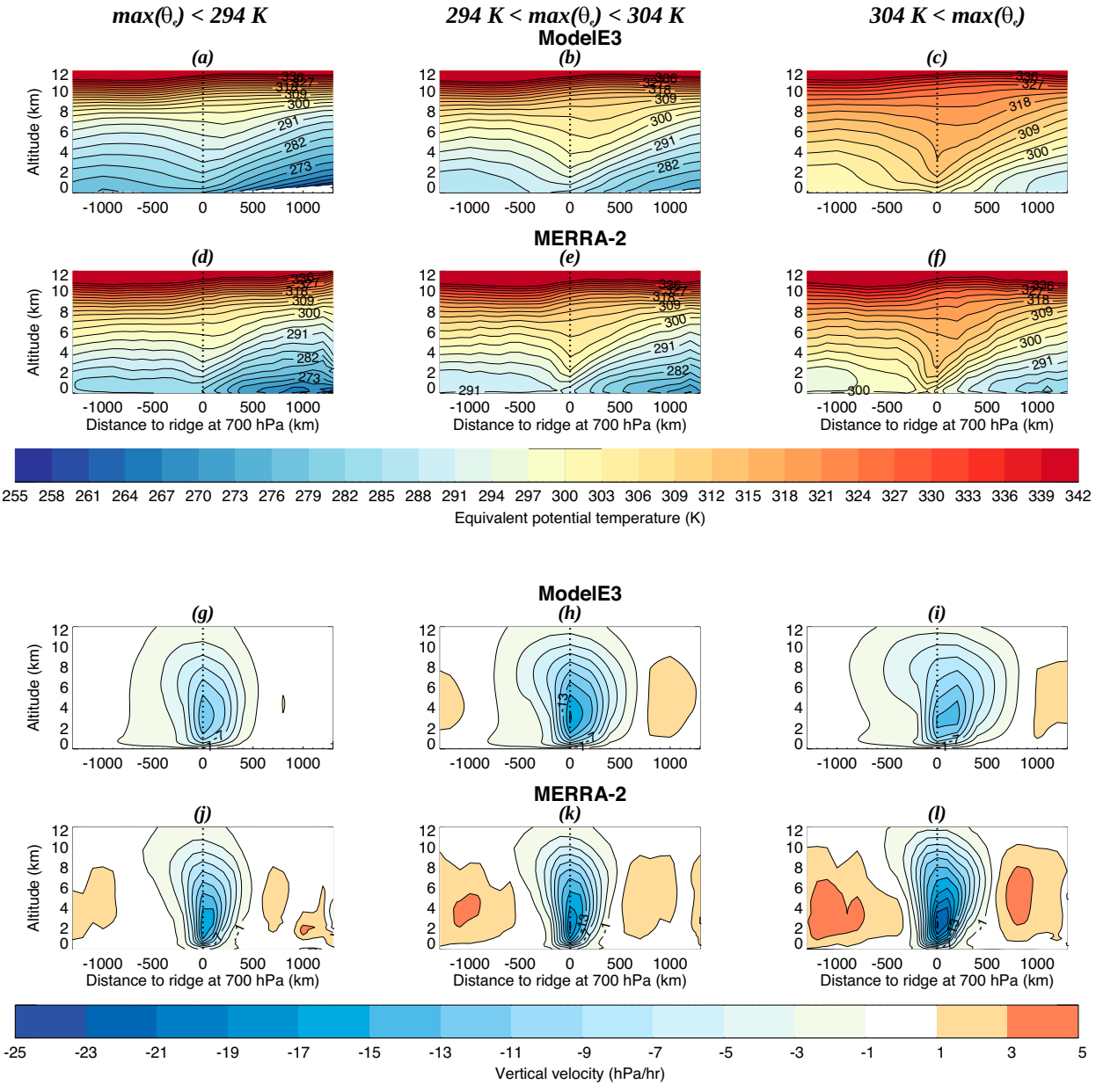

FIG. 7. Composite transects across the thermal ridge of (a)–(f) θ_e and (g)–(l) vertical velocity for (a)–(c) and (g)–(i) model E3 and (d)–(f) and (j)–(l) MERRA-2 for three categories from (a),(d),(g),(j) $\theta_e < 294$ K, (b),(e),(h),(k) $294 < \theta_e < 304$ K, and (c),(f),(i),(l) $\theta_e > 304$ K. In each subplot, the vertical dashed line marks the location of the thermal ridge at 700 hPa, the x axis is the distance to the ridge (km), and the y axis is the altitude (km).

coldest max(θ_e) category; Fig. 7g vs Fig. 7j]. This may be due to the coarser spatial resolution of E3 compared to MERRA-2. However, the reanalysis indicates that vertical velocities are the strongest for the warmest max(θ_e) category, while the model produces the greatest ascent strength for the medium max(θ_e) category. To test whether this discrepancy might have consequences for clouds and precipitation in the thermal ridge, which in turn would affect latent heat release as well as its impact on occlusion persistence and overall evolution, we next examine composite transects of cloud fraction.

Using model E3 profiles of cloud fraction, we build composite transects following the same method used for θ_e and ω transects. The model cloud fraction is computed as the sum of convective and stratiform cloud fraction (including precipitation fraction) as viewed by the model radiation scheme. As discussed previously, the observed profiles are not evenly distributed in space and instead are provided along the satellite's orbit (cf. section 2e; Naud et al. 2024). Therefore, we only sample some portion of the thermal ridge area for each case. In Naud et al. (2024), it is shown that by compositing multiple

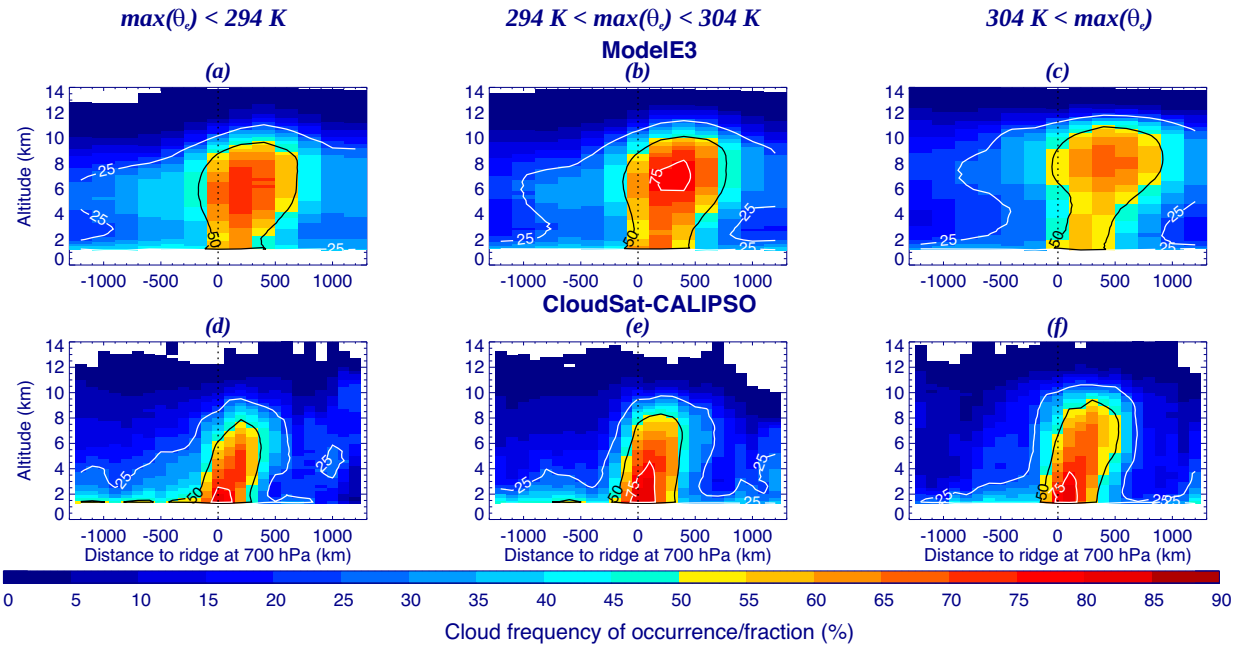

FIG. 8. (a)–(c) Composite transect of model E3 cloud fraction across the thermal ridge for three θ_e categories and (d)–(f) corresponding transects of *CloudSat–CALIPSO* cloud frequency of occurrence. (a),(d) Thermal ridges with θ_e at 700 hPa < 294 K, (b),(e) $294 < \theta_e <$ 304 K, and (c),(f) 304 K $< \theta_e$. In each panel, the vertical dotted line indicates the location of the thermal ridge, and the solid black and white contours indicate the 25%, 50%, and 75% fraction/frequency levels.

cases the impact of this sparse coverage can be alleviated. The observation-based composite transects are the sum of all observed profiles of the hydrometeor mask (with 1 s where GEOPROF-lidar indicates a cloud layer and 0 s otherwise) normalized by the total number of profiles. The result is a frequency of hydrometeor occurrence across the thermal ridge. Some differences between E3 and observations can arise due to precipitation contamination in the observations attenuating radar signals to such an extent that hydrometeors at lower altitudes are not observable.

Figure 8 shows the composite transects of the E3 cloud fraction per max(θ_e) category and the corresponding transects of hydrometeor frequency of occurrence obtained from *CloudSat–CALIPSO*. Regarding simulated versus observed hydrometeor transects for each max(θ_e) category independently, E3 exhibits larger cloud fractions above 8 km than observed along with a tendency to expand further poleward at those altitudes as well. This is true for all three max(θ_e) categories. At those altitudes, the *CALIPSO* lidar is less often attenuated and the observations are quite accurate as a result. Therefore, it is probable that the E3 overestimation of cloud fraction (by at least 5%–10%) is a robust result at those higher altitudes. In contrast to the higher-altitude results, *CloudSat–CALIPSO* displays a maximum in hydrometeor frequency at low altitudes (below 5 km), where only the radar can sense hydrometeors and where precipitating hydrometeors tend to be more frequent.

Despite these differences in overall distribution, the model does reproduce the contrasts between max(θ_e) categories in accord with observations: Cloud tops expand upward and poleward from low to high θ_e categories. As previously reported in Naud et al. (2024) for the observations, the maximum cloud fraction in the largest θ_e category is less than that of the middle θ_e category. However, the drop in maximum cloud fraction from medium to high max(θ_e) ridges is more dramatic in E3 than observed (in fact, it is barely noticeable in the observed transects), which is possibly exacerbated by the concurrent drop in ascent strength that only E3 produces.

Because cloud fraction only describes where and when clouds form, it does not relay information regarding how tenuous those clouds might be. Therefore, we analyze a different diagnostic of the cloud state: composite transects of ice water content. These data are provided by the 2C-ICE product, and we utilize the same compositing strategy as that used for hydrometeor frequency; i.e., the vertical profiles of hydrometeor presence/absence are replaced with profiles of ice water content. To separate out the impact of changing hydrometeor frequency from one max(θ_e) category to the next, ice water content is only averaged where ice is present, i.e., IWC > 0 gm^{-3}. Because 2C-ICE relies on a combination of information from both lidar and radar, greater uncertainties are expected in cloud areas where only one of the two instruments can detect hydrometeors. The lidar signal is superior at detecting small particles often found near cloud top that the radar cannot detect, and inversely, the lidar signal gets attenuated in thick clouds leaving radar reflectivities solely available at lower altitudes (Deng et al. 2010). Profiles of E3 IWC are composited with the same method used for the other variables, as described, but after a reset of IWC to zero if below the thresholds discussed in section 2d. The model provides ice mass for both stratiform and convective clouds, including precipitating components. Here, we use the sum of all four components.

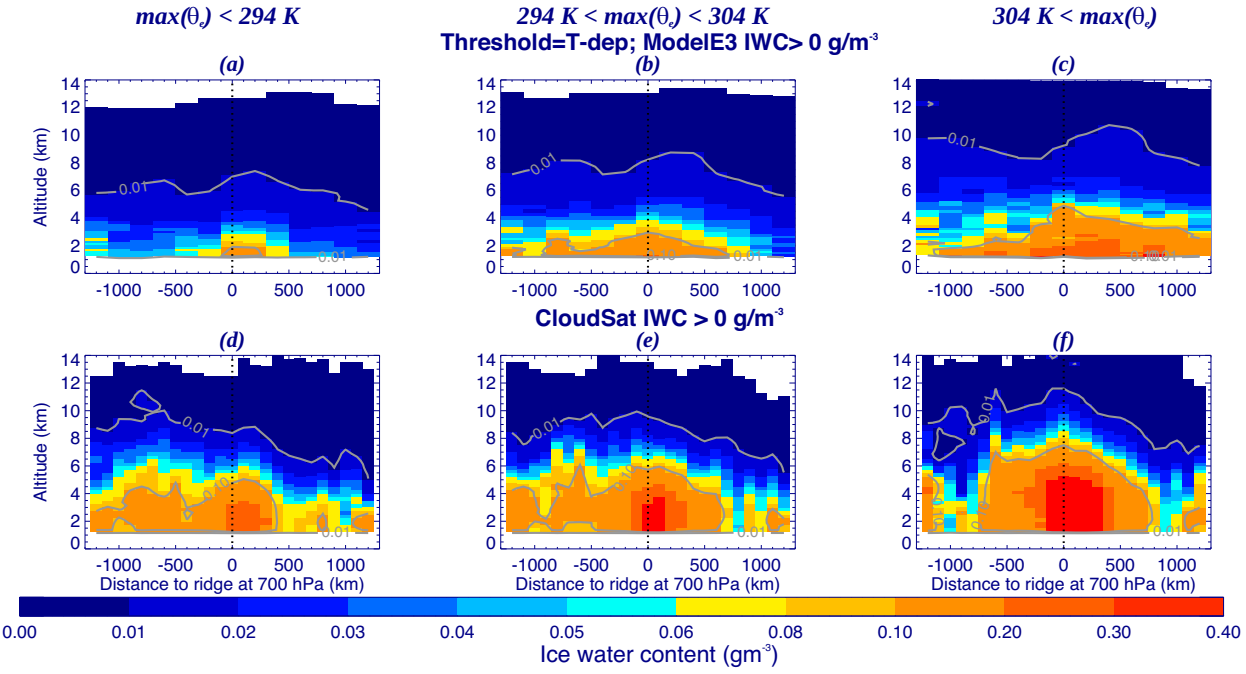

FIG. 9. Composite transects of conditional IWC (i.e., average over all scenes for IWC > 0) from (a)–(c) model E3 and (d)–(f) *CloudSat–CALIPSO* (2C-ICE) for the three thermal ridge categories: (a),(d) max(θ_e) < 294 K, (b),(e) 294 < max(θ_e) < 304, and (c),(f) 304 K < max(θ_e). In each panel, the vertical dashed line represents the location of the thermal ridge at 700 hPa. The light gray contours show the 0.01 and 0.1 gm^{-3} IWC levels.

For each max(θ_e) category, model E3 simulates lower values of IWC than reported from 2C-ICE (Fig. 9). However, the overall distribution of IWC with altitude exhibits a more realistic pattern than the cloud fraction, with larger mass at lower rather than higher altitudes, as would be expected in environments where available moisture is maximized at lower levels. Below the 50% model cloud occurrence level (cf. at levels below the solid black line in Figs. 8a–c), while the model reproduces the variations in IWC across the ridge, with a maximum at and poleward of the ridge, the overall magnitude is less than observed. This implies that E3 produces clouds too often but with less ice than observed. This too many, too tenuous high-level cloud bias is in contrast to what has often been reported in most ESM analyses at lower altitudes: the "too few, too bright" cloud problem (e.g., Nam et al. 2012; Konsta et al. 2022). At lower altitudes with a temperature range where mixed phases occur, biases could be reflective of differences in temperature thresholds for assumed ice–liquid partitioning in *CloudSat–CALIPSO* versus the GISS model: For the latter, liquid extends to colder temperatures, thus lower ice cloud fractions.

For occlusions in general, simulated and observed transects reveal a clear increase in IWC from low to medium to high max(θ_e) thermal ridges. Therefore, while the warmest thermal ridges may have less frequent clouds than their slightly "cooler" counterparts, they do contain more ice, which is consistent with larger precipitation rates as reported in Naud et al. (2024). Remarkably, the model represents these contrasts well, lending confidence that it reproduces the moist processes in these occluded systems in a fairly realistic way. However, the lower IWC overall implies insufficient modeled latent heating, which could contribute to the weaker PV erosion aloft and possibly the lower overall occurrence of occlusions.

4. Discussion

Analyses thus far have verified that 1) an ESM can produce occluded cyclones, and 2) it does so with realistic thermal and kinematic structures, but 3) with some possible biases in the representation of ascent strength, cloud coverage, and ice mass. While these issues may connect to the number of occluded cyclones, their location, and their longevity, they do not impair the ability of the model to represent a realistic sensitivity of clouds in the thermal ridge to the thermodynamic characteristics of the thermal ridge. However, we have not demonstrated the importance of this ability in a climatological context and why further improvements in the simulation of clouds and precipitation in the model are necessary. To this end, we begin by exploring the mean precipitation in E3 cyclones that have reached their peak intensity—separating such cyclones into those that, at some point in their life cycles, occlude and those that never do (according to the identification method outlined in section 2d). One caveat is that the occlusion identification method is conservative. It is designed to excel at identifying cyclones that are occluded but tend to reject ambiguous cases. Therefore, a small number of cyclones at peak intensity categorized as "unoccluded" may arguably be occluded.

Cyclone-centered composites of surface precipitation are constructed for each subset of cyclones (Figs. 10a,b). These

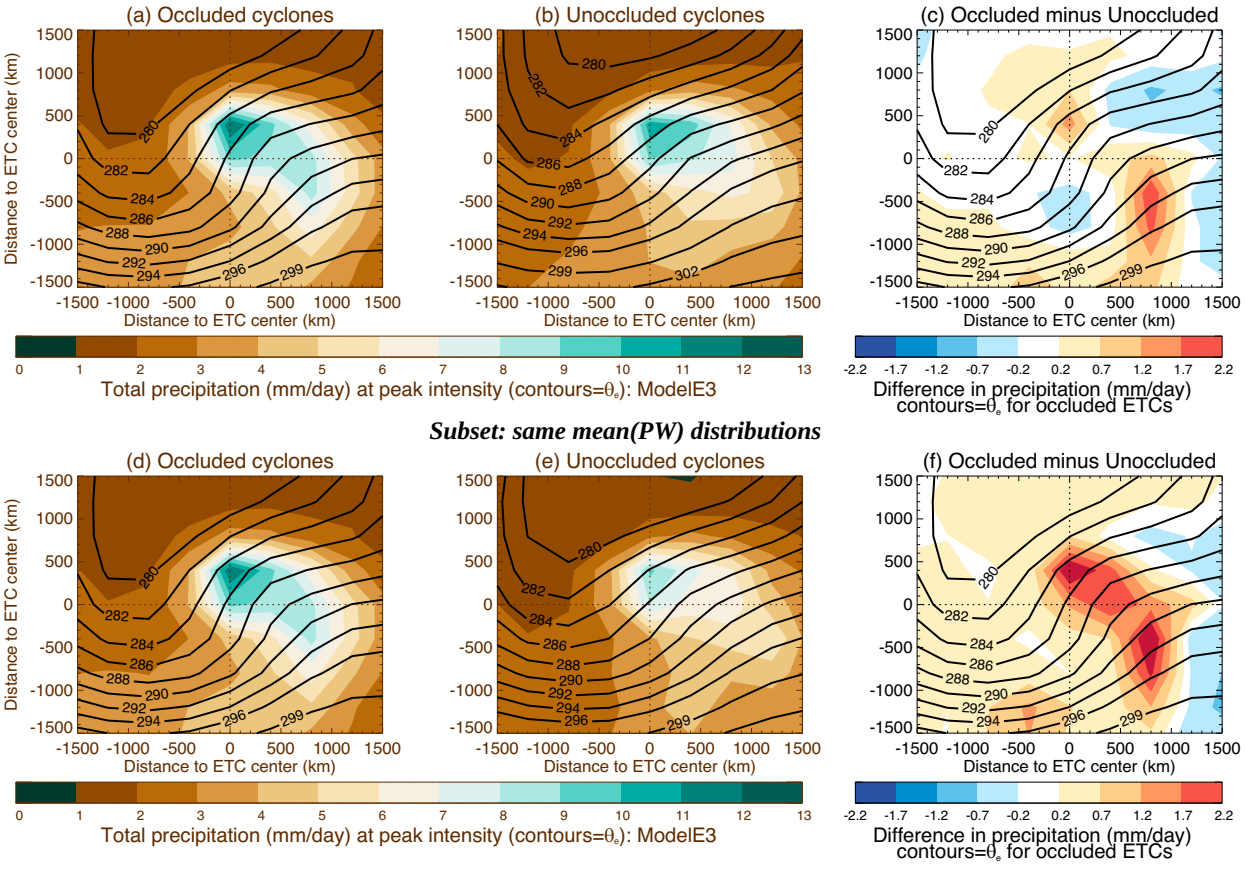

FIG. 10. Cyclone-centered composites of E3 surface precipitation rates (in color) for (a) occluded cyclones and (b) unoccluded cyclones at peak intensity, with a solid contour showing their associated composite of the equivalent potential temperature (in 2-K intervals from 280 K). (c) Difference in precipitation between occluded and unoccluded cyclones, with solid contours showing the composite of the equivalent potential temperature of occluded cyclones. (d)–(f) Similar composites as in (a)–(c), but for a subset of cyclones at peak intensity for which both occluded and unoccluded subsets share the same distribution of mean (PW) across cyclones. The dotted lines intersect at the cyclone's center.

composites reveal that in E3, cyclones that do occlude produce more precipitation than those that do not, with differences up to 1.5–2 mm day^{-1} at the locations where cyclones in general produce most of the precipitation (Fig. 10c), i.e., northwest of the cyclone center (i.e., the TROWAL region) and the precold frontal (warm sector) region. However, further analysis revealed that the set of unoccluded cyclones includes a greater fraction of systems with large mean precipitable water (PW) in their environments (22% have PW > 13 mm, compared to 6% of occluded cyclones). This is likely related to the tendency for E3 occluded cyclones to occur frequently at high latitudes, away from the high PW reservoir, while unoccluded cyclones have a more widespread latitude distribution. PW and precipitation are highly correlated in cyclones (e.g., Field and Wood 2007; Booth et al. 2018; Sinclair and Catto 2023); thus, we sort the two sets of cyclones to force the mean cyclone-wide PW distribution across all cyclones in each subset to match. This is achieved by randomly removing cyclones from each set until both sets include the same number of cyclones with a given mean PW within 1 mm. For these two sets of occluded and unoccluded cyclones with matching PW distributions, the difference in precipitation is much larger, as might be expected, but not previously documented (Figs. 10d–f). This suggests that E3 occluded cyclones are more efficient at processing PW into precipitation. Preliminary tests made using a similar stratification of precipitation observations (not shown) confirm that occluded cyclones are, indeed, more efficient at precipitation production. The full details of this analysis will be presented in a forthcoming paper. This result demonstrates that occluded cyclones play an important role in the production of precipitation and its extremes and that ESMs must faithfully reproduce this stage in the cyclone life cycle to accurately represent precipitation totals, their future changes, and their extremes.

5. Conclusions

Using a novel method for identifying extratropical cyclones that undergo an occlusion, the most recent version of the GISS Earth system model (E3) was tested for its ability to represent occlusions, their structure, and their associated cloud field. Though

model E3 can simulate the occlusion process, compared to the MERRA-2 reanalysis, it tends to 1) underestimate the number of tracks with occlusion, 2) place the occlusions too far poleward, and 3) simulate long-duration occlusions too often. However, the thermal and kinematic structures of the model's occluded cyclones and attendant thermal ridges are reasonably well depicted. An analysis of *CloudSat–CALIPSO* GEOPROF-lidar hydrometeor retrievals against E3 reveals that the E3 cloud distribution across thermal ridges, while displaying a reasonable sensitivity to the thermal ridge characteristics, tends to be top heavy; i.e., the model has a tendency to produce high clouds too frequently and over a wider area than suggested by satellite data. When ice water content transects are compared to *CloudSat–CALIPSO* 2C-ICE retrievals, a more realistic vertical distribution of condensate amounts is produced by E3, albeit with less ice than observed. This issue of too many, too tenuous high-level clouds is not unique to E3 (e.g., Naud et al. 2019) and should inform needed model developments as modeling centers prepare for CMIP7.

Further work will be necessary to establish the root cause of this issue, which could be conducted by using the other members of the calibrated physics ensemble developed for E3 (Elsaesser et al. 2024). In the ensemble, the physics is the same across models, but the various parameters used for tuning are not. An intercomparison of the different members could help establish whether these issues stem from the tuning parameter settings. Also, known issues in E3's parameterization schemes could impact cloud fraction and ice amounts at high altitudes in thermal ridges: 1) a too-weak sink term of stratiform anvil cloud area (possibly arising from insufficient IWC seeding stratiform rainfall; Elsaesser et al. 2022) and 2) an overactive detrainment of slowly sedimenting small-ice particles from any embedded convective clouds (e.g., Elsaesser et al. 2017a).

Extratropical cyclones need to be well represented in ESMs because of their important role in the meridional transport of heat and moisture, as well as in the production of precipitation and its extremes. Here, using E3 cyclone-centered precipitation, we demonstrate that the life cycle of these systems also requires adequate representation because occluded cyclones in the model are a lot more efficient at converting moisture into precipitation compared to cyclones that never occlude. The next step will be to use E3 to explore occluded cyclones in a warmer climate with the goal of quantifying how an increased global temperature might influence the occlusion process and associated precipitation. As the resolution and sophistication of ESMs increase, the impact of microphysical processes on occlusions and how they might be represented in models will also benefit from increased scrutiny. Such efforts will be aided by adding more vertically resolved observations and improved IWC and particle size measurements in general, such as those jointly retrieved from the radar and microwave radiometer aboard GPM, retrievals from in-development ice-sensing satellite missions [e.g., the Polarized Submillimeter Ice-Cloud Radiometer (PolSIR) sampling the most equatorward cyclone-associated ice clouds], and radar and lidar data from the European Space Agency Earth Cloud, Aerosol, and Radiation Explorer (EarthCARE) mission (Illingworth et al. 2015).

Acknowledgments. The work was funded by the NASA *CloudSat–CALIPSO* science team recompete program, Grant 80NSSC20K0085. CMN and DJP received additional funding from the NASA Modeling, Analysis, and Prediction (MAP) program, Grant 80NSSC21K1728 and GSE from the NASA MAP Program and APAM-GISS Cooperative Agreement 80NSSC18M0133, NASA Precipitation Measurement Missions Grant 80NSSC22K0609, and the NASA PolSIR Project (80LARC24CA001). A portion of this research was conducted at the Jet Propulsion Laboratory, California Institute of Technology, under a contract with the National Aeronautics and Space Administration (NASA) 80NM0018D0004. Computing resources for the work were provided by the NASA High-End Computing (HEC) program through the NASA Center for Climate Simulation (NCCS) at the Goddard Space Flight Center. The authors thank Min Deng and Matthew Lebsock for their detailed information on *CloudSat* and *CALIPSO* measurements and products and three anonymous reviewers for their insightful comments that greatly helped improve this manuscript.

Data availability statement. The MERRA-2 database of occluded cyclones and the ERA-Interim database of cyclones are accessible at https://data.giss.nasa.gov/storms/obs-etc/. *CloudSat–CALIPSO* 2B-GEOPROF-lidar and 2C-ICE data files are documented and available at https://www.cloudsat.cira.colostate.edu/. MERRA-2 profiles of temperature, specific humidity, wind, and vertical velocity information are available at Global Modeling and Assimilation Office (GMAO) (2015), MERRA-2 inst3_3d_asm_Np: 3d, 3-Hourly, Instantaneous, Pressure-Level, Assimilation, Assimilated Meteorological Fields V5.12.4, Greenbelt, MD, USA, Goddard Earth Sciences Data and Information Services Center (GES DISC), accessed: January 2020, https://doi.org/10.5067/QBZ6MG944HW0; and Global Modeling and Assimilation Office (GMAO) (2015), MERRA-2 inst6_3d_ana_Np: 3d, 6-Hourly, Instantaneous, Pressure-Level, Analysis, Analyzed Meteorological Fields V5.12.4, Greenbelt, MD, USA, Goddard Earth Sciences Data and Information Services Center (GES DISC), accessed: January 2020, https://doi.org/10.5067/A7S6XP56VZWS.

REFERENCES

Bauer, M., and A. D. Del Genio, 2006: Composite analysis of winter cyclones in a GCM: Influence on climatological humidity. *J. Climate*, **19**, 1652–1672, https://doi.org/10.1175/JCLI3690.1.

——, G. Tselioudis, and W. B. Rossow, 2016: A new climatology for investigating storm influences in and on the extratropics. *J. Appl. Meteor. Climatol.*, **55**, 1287–1303, https://doi.org/10.1175/JAMC-D-15-0245.1.

Bengtsson, L., K. I. Hodges, and N. Keenlyside, 2009: Will extratropical storms intensify in a warmer climate? *J. Climate*, **22**, 2276–2301, https://doi.org/10.1175/2008JCLI2678.1.

Binder, H., M. Boettcher, H. Joos, and H. Wernli, 2016: The role of warm conveyor belts for the intensification of extratropical cyclones in Northern Hemisphere winter. *J. Atmos. Sci.*, **73**, 3997–4020, https://doi.org/10.1175/JAS-D-15-0302.1.

Booth, J. F., C. M. Naud, and J. Willison, 2018: Evaluation of extratropical cyclone precipitation in the North Atlantic basin: An analysis of ERA-Interim, WRF, and two CMIP5 models.

J. Climate, **31**, 2345–2360, https://doi.org/10.1175/JCLI-D-17-0308.1.

Bretherton, C. S., and S. Park, 2009: A new moist turbulence parameterization in the Community Atmosphere Model. *J. Climate*, **22**, 3422–3448, https://doi.org/10.1175/2008JCLI2556.1.

Catto, J. L., C. Jakob, G. Berry, and N. Nicholls, 2012: Relating global precipitation to atmospheric fronts. *Geophys. Res. Lett.*, **39**, L10805, https://doi.org/10.1029/2012GL051736.

——, ——, and N. Nicholls, 2015: Can the CMIP5 models represent winter frontal precipitation? *Geophys. Res. Lett.*, **42**, 8596–8604, https://doi.org/10.1002/2015GL066015.

Cesana, G., A. D. Del Genio, A. S. Ackerman, M. Kelley, G. Elsaesser, A. M. Fridlind, Y. Cheng, and M.-S. Yao, 2019: Evaluating models' response of tropical low clouds to SST forcings using CALIPSO observations. *Atmos. Chem. Phys.*, **19**, 2813–2832, https://doi.org/10.5194/acp-19-2813-2019.

Cesana, G. V., A. S. Ackerman, A. M. Fridlind, I. Silber, and M. Kelley, 2021: Snow reconciles observed and simulated phase partitioning and increases cloud feedback. *Geophys. Res. Lett.*, **48**, e2021GL094876, https://doi.org/10.1029/2021GL094876.

Cheng, Y., and Coauthors, 2020: A second-order closure turbulence model: New heat flux equations and no critical Richardson number. *J. Atmos. Sci.*, **77**, 2743–2759, https://doi.org/10.1175/JAS-D-19-0240.1.

Crocker, A., W. L. Godson, and C. M. Penner, 1947: Frontal contour charts. *J. Meteor.*, **4**, 95–99, https://doi.org/10.1175/1520-0469(1947)004%3C0095:FCCBPO%3E2.0.CO;2.

Dee, D. P., and Coauthors, 2011: The ERA-Interim reanalysis: Configuration and performance of the data assimilation system. *Quart. J. Roy. Meteor. Soc.*, **137**, 553–597, https://doi.org/10.1002/qj.828.

Del Genio, A. D., J. Wu, A. B. Wolf, Y. Chen, M. Yao, and D. Kim, 2015: Constraints on cumulus parameterization from simulations of observed MJO events. *J. Climate*, **28**, 6419–6442, https://doi.org/10.1175/JCLI-D-14-00832.1.

Deng, M., G. G. Mace, Z. Wang, and H. Okamoto, 2010: Tropical Composition, Cloud and Climate Coupling Experiment validation for cirrus cloud profiling retrieval using CloudSat radar and CALIPSO lidar. *J. Geophys. Res.*, **115**, D00J15, https://doi.org/10.1029/2009JD013104.

——, G. G. Gerald, Z. Wang, and R. P. Lawson, 2013: Evaluation of several A-train ice cloud retrieval products with in situ measurements collected during the SPARTICUS Campaign. *J. Appl. Meteor. Climatol.*, **52**, 1014–1030, https://doi.org/10.1175/JAMC-D-12-054.1.

Elsaesser, G. S., A. D. Del Genio, J. H. Jiang, and M. van Lier-Walqui, 2017a: An improved convective ice parameterization for the NASA GISS global climate model and impacts on cloud ice simulation. *J. Climate*, **30**, 317–336, https://doi.org/10.1175/JCLI-D-16-0346.1.

——, C. W. O'Dell, M. D. Lebsock, R. Bennartz, T. J. Greenwald, and F. J. Wentz, 2017b: The Multisensor Advanced Climatology of Liquid Water Path (MAC-LWP). *J. Climate*, **30**, 10 193–10 210, https://doi.org/10.1175/JCLI-D-16-0902.1.

——, R. Roca, T. Fiolleau, A. D. Del Genio, and J. Wu, 2022: A simple model for tropical convective cloud shield area growth and decay rates informed by geostationary IR, GPM, and Aqua/AIRS satellite data. *J. Geophys. Res. Atmos.*, **127**, e2021JD035599, https://doi.org/10.1029/2021JD035599.

——, and Coauthors, 2024: Using machine learning to generate a GISS ModelE Calibrated Physics Ensemble (CPE). ESS Open Archive, https://doi.org/10.22541/essoar.172745119.96698579/v1.

Field, P. R., and R. Wood, 2007: Precipitation and cloud structure in midlatitude cyclones. *J. Climate*, **20**, 233–254, https://doi.org/10.1175/JCLI3998.1.

Gelaro, R., and Coauthors, 2017: The Modern-Era Retrospective Analysis for Research and Applications, Version 2 (MERRA-2). *J. Climate*, **30**, 5419–5454, https://doi.org/10.1175/JCLI-D-16-0758.1.

Gettelman, A., and H. Morrison, 2015: Advanced two-moment bulk microphysics for global models. Part I: Off-line tests and comparison with other schemes. *J. Climate*, **28**, 1268–1287, https://doi.org/10.1175/JCLI-D-14-00102.1.

Grim, J. A., R. M. Rauber, M. K. Ramamurthy, B. F. Jewett, and M. Han, 2007: High-resolution observations of the Trowal–warm-frontal region of two continental winter cyclones. *Mon. Wea. Rev.*, **135**, 1629–1646, https://doi.org/10.1175/MWR3378.1.

Han, M., R. M. Rauber, M. K. Ramamurthy, B. F. Jewett, and J. A. Grim, 2007: Mesoscale dynamics of the Trowal and warm-frontal regions of two continental winter cyclones. *Mon. Wea. Rev.*, **135**, 1647–1670, https://doi.org/10.1175/MWR3377.1.

Hawcroft, M. K., L. C. Shaffrey, K. I. Hodges, and H. F. Dacre, 2012: How much Northern Hemisphere precipitation is associated with extratropical cyclones? *Geophys. Res. Lett.*, **39**, L24809, https://doi.org/10.1029/2012GL053866.

Hersbach, H., and Coauthors, 2020: The ERA5 global reanalysis. *Quart. J. Roy. Meteor. Soc.*, **146**, 1999–2049, https://doi.org/10.1002/qj.3803.

Hoskins, B. J., and K. I. Hodges, 2002: New perspectives on the Northern Hemisphere winter storm tracks. *J. Atmos. Sci.*, **59**, 1041–1061, https://doi.org/10.1175/1520-0469(2002)059<1041:NPOTNH>2.0.CO;2.

Illingworth, A. J., and Coauthors, 2015: The EarthCARE satellite: The next step forward in global measurements of clouds, aerosols, precipitation, and radiation. *Bull. Amer. Meteor. Soc.*, **96**, 1311–1332, https://doi.org/10.1175/BAMS-D-12-00227.1.

Jewell, R., 1981: Tor Bergeron's first year in the Bergen school: Towards an historical appreciation. *Weather and Weather Maps: A Volume Dedicated to the Memory of Tor Bergeron*, Contributions to Current Research in Geophysics, Vol. 10, Birkhäuser Basel, 474–490.

Kelley, M., and Coauthors, 2020: GISS-E2.1: Configurations and climatology. *J. Adv. Model. Earth Syst.*, **12**, e2019MS002025, https://doi.org/10.1029/2019MS002025.

Konsta, D., and Coauthors, 2022: Low-level marine tropical clouds in six CMIP6 models are too few, too bright but also too compact and too homogeneous. *Geophys. Res. Lett.*, **49**, e2021GL097593, https://doi.org/10.1029/2021GL097593.

Kunkel, K. E., D. R. Easterling, D. A. R. Kristovich, B. Gleason, L. Stoecker, and R. Smith, 2012: Meteorological causes of the secular variations in observed extreme precipitation events for the conterminous United States. *J. Hydrometeor.*, **13**, 1131–1141, https://doi.org/10.1175/JHM-D-11-0108.1.

——, and Coauthors, 2013: Monitoring and understanding trends in extreme storms: State of knowledge. *Bull. Amer. Meteor. Soc.*, **94**, 499–514, https://doi.org/10.1175/BAMS-D-11-00262.1.

Li, J.-L. F., G. V. Cesana, K.-M. Xu, M. Richardson, H. Takahashi, and J. Jiang, 2023: Comparisons of simulated radiation, surface wind stress and SST fields over tropical pacific by the GISS CMIP6 versions of global climate models with observations. *Environ. Res. Commun.*, **5**, 015005, https://doi.org/10.1088/2515-7620/aca9ab.

Mace, G. G., and Q. Zhang, 2014: The CloudSat radar-lidar geometrical profile product (RL-GeoProf): Updates, improvements,

and selected results. *J. Geophys. Res. Atmos.*, **119**, 9441–9462, https://doi.org/10.1002/2013JD021374.

——, ——, M. Vaughan, R. Marchand, G. Stephens, C. Trepte, and D. Winker, 2009: A description of hydrometeor layer occurrence statistics derived from the first year of merged CloudSat and CALIPSO data. *J. Geophys. Res.*, **114**, D00A26, https://doi.org/10.1029/2007JD009755.

Marciano, C. G., G. M. Lackmann, and W. A. Robinson, 2015: Changes in U.S. East Coast cyclone dynamics with climate change. *J. Climate*, **28**, 468–484, https://doi.org/10.1175/JCLI-D-14-00418.1.

Martin, J. E., 1998a: The structure and evolution of a continental winter cyclone. Part I: Frontal structure and the occlusion process. *Mon. Wea. Rev.*, **126**, 303–328, https://doi.org/10.1175/1520-0493(1998)126<0303:TSAEOA>2.0.CO;2.

——, 1998b: The structure and evolution of a continental winter cyclone. Part II: Frontal forcing of an extreme snow event. *Mon. Wea. Rev.*, **126**, 329–348, https://doi.org/10.1175/1520-0493(1998)126<0329:TSAEOA>2.0.CO;2.

——, 1999a: Quasigeostrophic forcing of ascent in the occluded sector of cyclones and the Trowal airstream. *Mon. Wea. Rev.*, **127**, 70–88, https://doi.org/10.1175/1520-0493(1999)127<0070:QFOAIT>2.0.CO;2.

——, 1999b: The separate roles of geostrophic vorticity and deformation in the midlatitude occlusion process. *Mon. Wea. Rev.*, **127**, 2404–2418, https://doi.org/10.1175/1520-0493(1999)127<2404:TSROGV>2.0.CO;2.

Nam, C., S. Bony, J.-L. Dufresne, and H. Chepfer, 2012: The 'too few, too bright' tropical low-cloud problem in CMIP5 models. *Geophys. Res. Lett.*, **39**, L21801, https://doi.org/10.1029/2012GL053421.

Naud, C. M., J. F. Booth, J. Jeyaratnam, L. J. Donner, C. J. Seman, M. Zhao, H. Guo, and Y. Ming, 2019: Extratropical cyclone clouds in the GFDL climate model: Diagnosing biases and the associated causes. *J. Climate*, **32**, 6685–6701, https://doi.org/10.1175/JCLI-D-19-0421.1.

——, J. Jeyaratnam, J. F. Booth, M. Zhao, and A. Gettelman, 2020: Evaluation of modeled precipitation in oceanic extratropical cyclones using IMERG. *J. Climate*, **33**, 95–113, https://doi.org/10.1175/JCLI-D-19-0369.1.

——, J. E. Martin, P. Ghosh, G. Elsaesser, and D. Posselt, 2023: Automated identification of occluded sectors in midlatitude cyclones: Method and some climatological applications. *Quart. J. Roy. Meteor. Soc.*, **149**, 1990–2010, https://doi.org/10.1002/qj.4491.

——, P. Ghosh, J. E. Martin, G. S. Elsaesser, and D. J. Posselt, 2024: A CloudSat–CALIPSO view of cloud and precipitation in the occluded quadrants of extratropical cyclones. *Quart. J. Roy. Meteor. Soc.*, **150**, 1336–1356, https://doi.org/10.1002/qj.4648.

Neu, U., and Coauthors, 2013: IMILAST: A community effort to intercompare extratropical cyclone detection and tracking algorithms. *Bull. Amer. Meteor. Soc.*, **94**, 529–547, https://doi.org/10.1175/BAMS-D-11-00154.1.

Penner, C. M., 1955: A three-front model for synoptic analyses. *Quart. J. Roy. Meteor. Soc.*, **81**, 89–91, https://doi.org/10.1002/qj.49708134710.

Pfahl, S., and H. Wernli, 2012: Quantifying the relevance of cyclones for precipitation extremes. *J. Climate*, **25**, 6770–6780, https://doi.org/10.1175/JCLI-D-11-00705.1.

Posselt, D. J., and J. E. Martin, 2004: The effect of latent heat release on the evolution of a warm occluded thermal structure. *Mon. Wea. Rev.*, **132**, 578–599, https://doi.org/10.1175/1520-0493(2004)132<0578:TEOLHR>2.0.CO;2.

Russotto, R. D., and Coauthors, 2022: Evolution of tropical cyclone properties across the development cycle of the GISS-E3 global climate model. *J. Adv. Model. Earth Syst.*, **14**, e2021MS002601, https://doi.org/10.1029/2021MS002601.

Schultz, D. M., and G. Vaughan, 2011: Occluded fronts and the occlusion process: A fresh look at conventional wisdom. *Bull. Amer. Meteor. Soc.*, **92**, 443–466, https://doi.org/10.1175/2010BAMS3057.1.

Sinclair, V. A., and J. L. Catto, 2023: The relationship between extra-tropical cyclone intensity and precipitation in idealised current and future climates. *Wea. Climate Dyn.*, **4**, 567–589, https://doi.org/10.5194/wcd-4-567-2023.

Smith, R. N. B., 1990: A scheme for predicting layer clouds and their water content in a general circulation model. *Quart. J. Roy. Meteor. Soc.*, **116**, 435–460, https://doi.org/10.1002/qj.49711649210.

Stephens, G. L., and Coauthors, 2002: The CloudSat mission and the A-train: A new dimension of space-based observations of clouds and precipitation. *Bull. Amer. Meteor. Soc.*, **83**, 1771–1790, https://doi.org/10.1175/BAMS-83-12-1771.

Stoelinga, M. T., J. D. Locatelli, and P. V. Hobbs, 2002: Warm occlusions, cold occlusions, and forward-tilting cold fronts. *Bull. Amer. Meteor. Soc.*, **83**, 709–721, https://doi.org/10.1175/1520-0477(2002)083<0709:WOCOAF>2.3.CO;2.

Sutcliffe, R. C., 1947: A contribution to the problem of development. *Quart. J. Roy. Meteor. Soc.*, **73**, 370–383, https://doi.org/10.1002/qj.49707331710.

Winker, D. M., M. A. Vaughan, A. Omar, Y. Hu, K. A. Powell, Z. Liu, W. H. Hunt, and S. A. Young, 2009: Overview of the CALIPSO mission and CALIOP data processing algorithms. *J. Atmos. Oceanic Technol.*, **26**, 2310–2323, https://doi.org/10.1175/2009JTECHA1281.1.

Yettella, V., and J. E. Kay, 2017: How will precipitation change in extratropical cyclones as the planet warms? Insights from a large initial condition climate model ensemble. *Climate Dyn.*, **49**, 1765–1781, https://doi.org/10.1007/s00382-016-3410-2.

Zhang, Z., and B. A. Colle, 2017: Changes in extratropical cyclone precipitation and associated processes during the twenty-first century over eastern North America and the western Atlantic using a cyclone-relative approach. *J. Climate*, **30**, 8633–8656, https://doi.org/10.1175/JCLI-D-16-0906.1.